Deformation and Fracture of MMC Under Combined Loadings

D.W.A.Rees and M.Liddiard

Department of Manufacturing and Engineering Systems,
Brunel University, Uxbridge, Middlesex UB8 3PH.

ABSTRACT

This paper outlines the flow and fracture behaviour of 17% and 25% SiC particulate reinforced 2124 aluminium alloys under different stress systems. Tensile and compressive testing and SEM studies reveal marked differences in ductility and the fracture path between the two modes. Though the strengths are comparable the tensile behaviour is notch sensitive and thus more brittle. Tensile failure originates at defects and inclusions and spreads across transverse plane with limited plasticity. In contrast, greater compressive strains arise with sliding along the 45° plane of maximum shear. Interrupted testing showed that these failures occurred through linking of micro-voids formed around particles. These voids nucleate from matrix material failure under the high local strains induced within a dense, immobile dislocation field surrounding particles. An initial dislocation field already exists at these sites due to matrix distortion as the two components in the material cool at different rates from high-temperature processing. The applied strain serves to increase the density of dislocations and to decreases their mobility to the critical condition required for failure.

Combined torsion-tension and torsion-compression loadings were applied incrementally for two stress paths (i) radial and (ii) stepped. Pure torsion, tension and compression tests were conducted under incremental loading to establish the yield stresses and the hardening behaviour for the mmc in its low and higher strain ranges. The results of all tests show that the yield locus for the material obeys a Mises description. The deformation behaviour is compared with that predicted from the Prandtl-Reuss plasticity theory. Regions of elasticity are apparent for both paths. However, the shear moduli under path (ii) appeared to be increased by larger magnitudes of axial stress in both senses. Flow beyond the yield point under (i) and (ii) reveals parabolic hardening and consistency with the normality rule but the material is essentially brittle under all loadings except compression. This points to a the use of a more appropriate flow theory modified with a damage parameter sensitive to the sense of the stress.

1. INTRODUCTION

Metal matrix composites originate from dispersion hardened alloys developed in the 1950's. Fibre-reinforced metals were introduced in the 60's but high production costs precluded their widespread use. There followed in the 70's the dual phase steels in which hard martensite particles were embedded in a softer ferritic matrix. This structure is similar to an mmc in

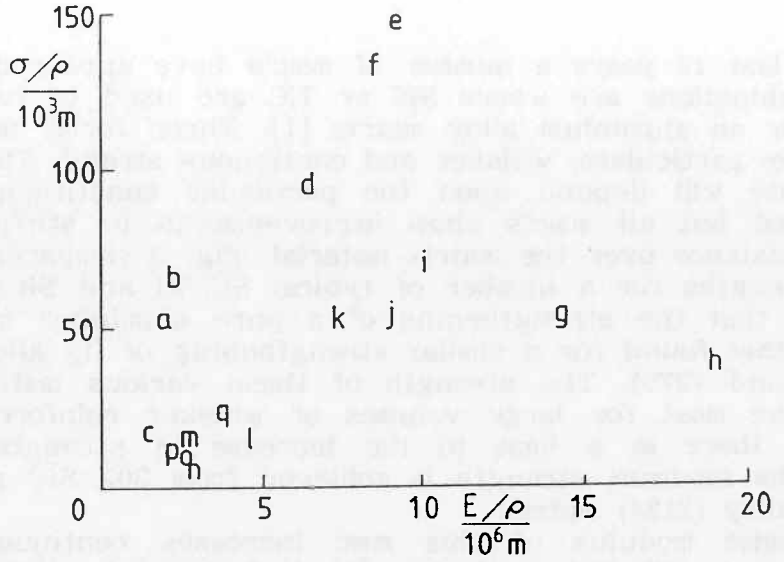

Fig. 1 Comparison between specific strength and specific stiffness in tension
(Key: a E glass/epoxy, b S glass/epoxy, c woven glass/epoxy, d kevlar/epoxy,
e carbon/epoxy, f carbon/peek, g carbon/polyimide...contd within Fig.2 caption)

which ceramic particles, whiskers or fibres are embedded in a metal or an alloy matrix. This combination provides good transverse properties, workability, low cost and weight. Their major advantage is the increase in stiffness and strength they can offer over certain other materials. The elastic moduli of mmc's lie between those of ceramics and metal alloys with comparable densities.

Fig. 1 shows a plot of specific tensile strength σ/ρ versus specific stiffness E/ρ for a range of materials. On this basis it is apparent that

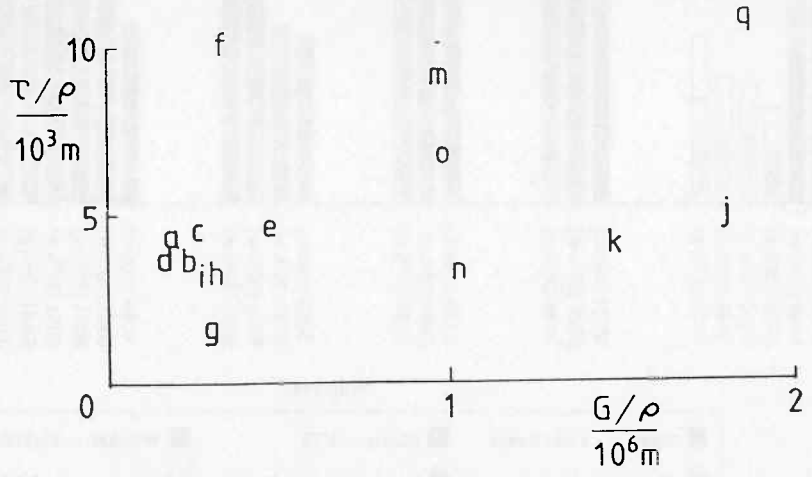

Fig. 2 Comparison between specific strength and specific stiffness in torsion.
(Key continued: h graphite/epoxy, i boron/epoxy, j boron/aluminium,k SiC/Al whisker,
l SiC/ceramic, m 2024 Al alloy, n 1025 steel, o Ti, p pine, q SiC/Al particulate)

mmc's (materials q and k) outperform wrought metals (m, n and o) in both modes. They do not match the strength of epoxy resins with uniaxial kevlar and carbon-fibres (d, e and f). The strengths of glass-fibre composites (a, b and c) are comparable to mmc's despite their reduced stiffness. Fig. 2 shows a plot of specific shear strength τ/ρ versus specific stiffness G/ρ for a similar range of materials. It is clear that mmc's (j, k and q) outperform many other materials in a shear mode. Though a uniaxial SiC reinforcement of mmc (material k) is better that the present particulate mmc (material q) under tension (Fig. 1) it offers no advantage under shear.

In the last 10 years a number of mmc's have appeared but the more common combinations are where SiC or TiC are used to reinforce a pure aluminium or an aluminium alloy matrix [1]. Three forms of reinforcement are available: particulate, whisker and continuous strand. The properties of the composite will depend upon the particular constituents and volume fraction used but all mmc's show improvenments in stiffness, wear and fracture resistance over the matrix material. Fig. 3 compares the yield and ultimate strengths for a number of typical SiC/Al and SiC/Al-alloy mmc's. This shows that the strengthening of a pure aluminium matrix (1100) is inferior to that found for a similar strengthening of its alloys (2024, 2124, 5083, 6061 and 7075). The strength of these various matrix materials is increased the most for large volumes of whisker reinforcement. Fig. 4a shows that there is a limit to the increase in strength that can be achieved. The maximum strength is achieved from 30% SiC particulate in a 4.5% Al-Cu alloy (2124) matrix.

The elastic modulus of this mmc increases continuously with the addition of up to 60% SiC particulate [2]. Unfortunately, these increases in strength and stiffness occur with a loss in tensile ductility of the composite (see Fig. 4b); this being a major limitation of all mmc's. The

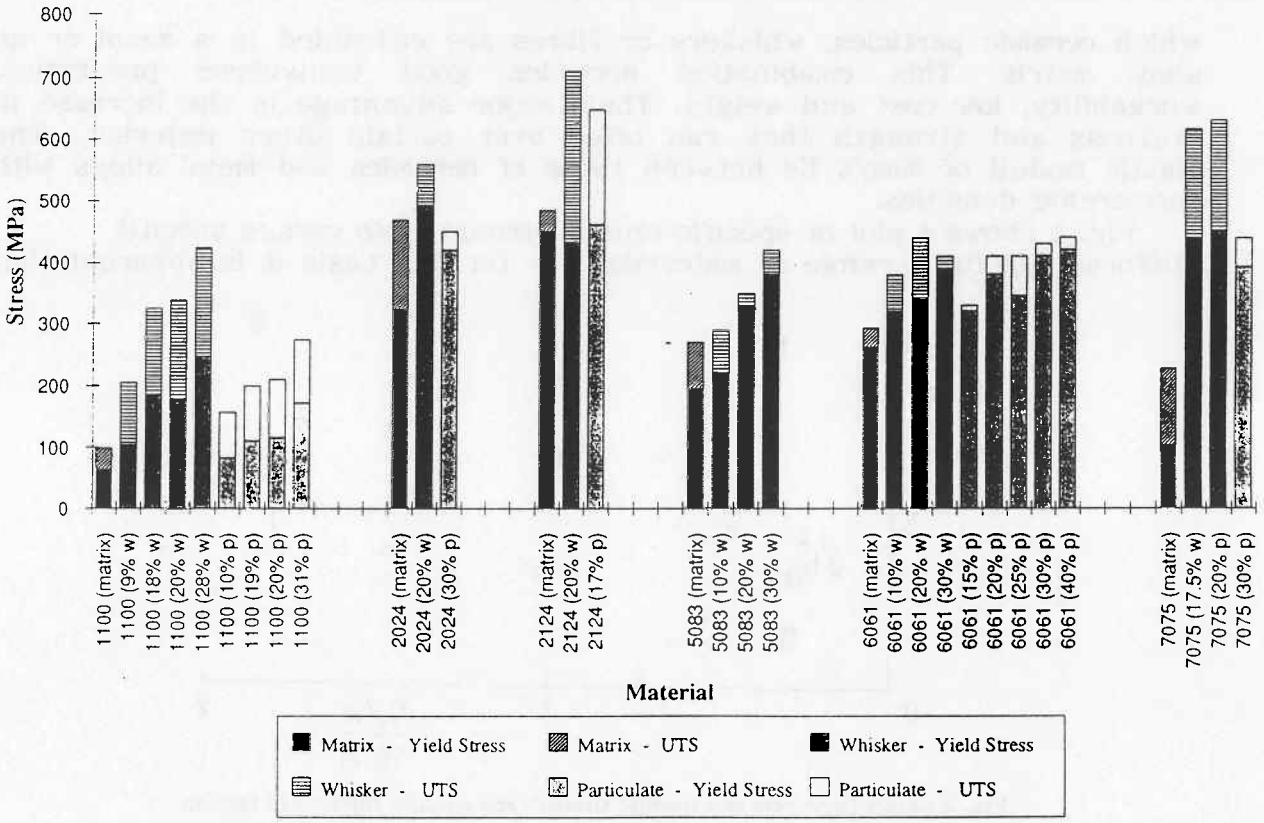

Fig. 3 The yield and ultimate strengths of SiC mmc's

present paper examines further the flow and fracture behaviour of an mmc with 17% and 25 % volumes of 3 μm SiC particles in a 2124 matrix. The mmc was manufactured by BP. A mixture of atomised aluminium powder and SiC particles is heated in an evacuated stainless steel chamber then isostatically compacted before extruding to a 1" diameter bar. To optimise its properties the bar requires solution treatment at 505°C for 1 hour, followed by a water quench and naturally ageing at room temperature for 7 days. This treatment was applied to oversized testpieces at a common intermediate stage of their manufacture.

The uniaxial studies were made to examine the influence of strain rate on compressive strength. SEM and acoustic emission techniques were used to establish the influence of mode of deformation upon the fracture mechanism. Etching and hardness testing reveal the size and distribution of the particles and the distortion of the surrounding matrix. A number of probable strengthening mechanisms are discussed. These will reveal that the improved strength of an mmc is controlled by the size and spacing of the particulates, the matrix grain size, dislocation density, sub-grain formation and strain hardening.

In practice, the stresses imposed by service loadings are likely to be complex. When safety factors are reduced to save weight the stresses in a material will approach the yield condition. In more conventional engineering

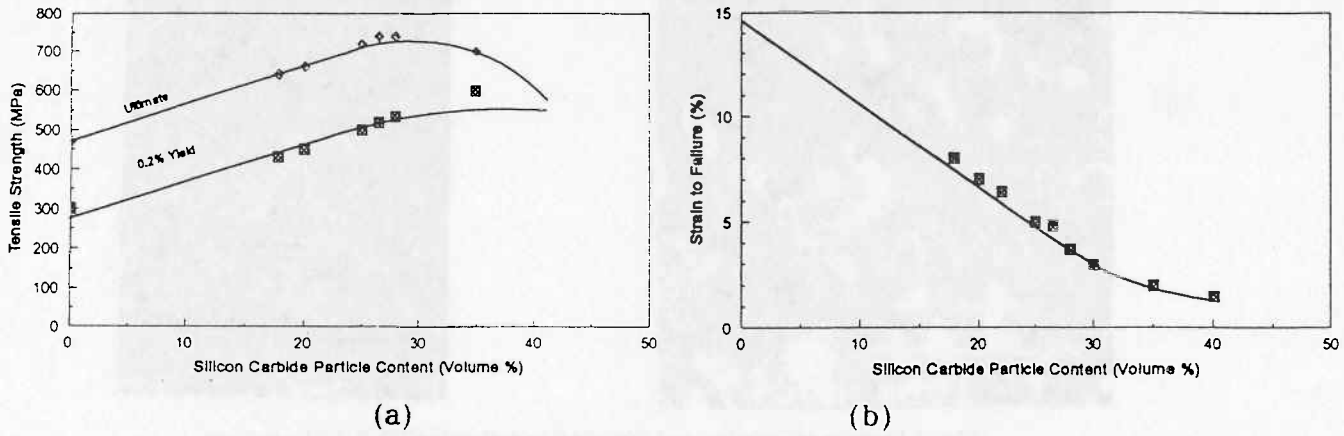

Fig. 4 Influence of volume fraction upon strength and ductility of extruded mmc

alloys plasticity will offer the safety margin required. The present study examines whether mmc's can be employed in a similar manner when operating close to the yield point under combined stress states. Results from combined tension-torsion experiments on the 25% particulate mmc are compared with the classical Prandtl-Reuss theory of plasticity [3,4]. There is evidence for a Mises plastic potential [5] and a rule of normality within the plastic range of an mmc but the range is much narrower than can be expected from wrought materials. It will be shown how a damage parameter can account for the extent to which void damage restricts the plastic flow.

2. MATERIAL CHARACTERISATION

2.1 Hardness

Heat treated samples of material were prepared by mounting in acrifix moulds and polishing to a 1 μm finish. Vickers indentations were made to enclose several particles under a 200 gm load. Micro-hardness tests of the matrix material were made under a 10 gm load. The respective tests gave comparable VPN's of 188.5 and 205 which shows that the matrix is hardened by the embedded particles beneath it.

2.2 Particle Size

Keller's reagent (concentrated acids: 1 ml HF, 1.5 ml HCl, 2.5 ml HNO_3 mixed with 95 ml of water) attacks the 2124 Al-alloy matrix preferentially. It can be used to reveal the grain boundary distortion and to expose the particle orientation and spacing. Preparation was similar to that described

for hardness testing. Etch times of 20, 40 and 120 secs left the SiC-particles untouched to reveal that their size varied between 2 and 5 μm. Fig. 5a shows their angular appearance and non-uniform distribution. For the longest etch time a reaction occurred between etchant and matrix producing a brittle chloride within shallow surface cracks around the particles (see Fig. 5b).

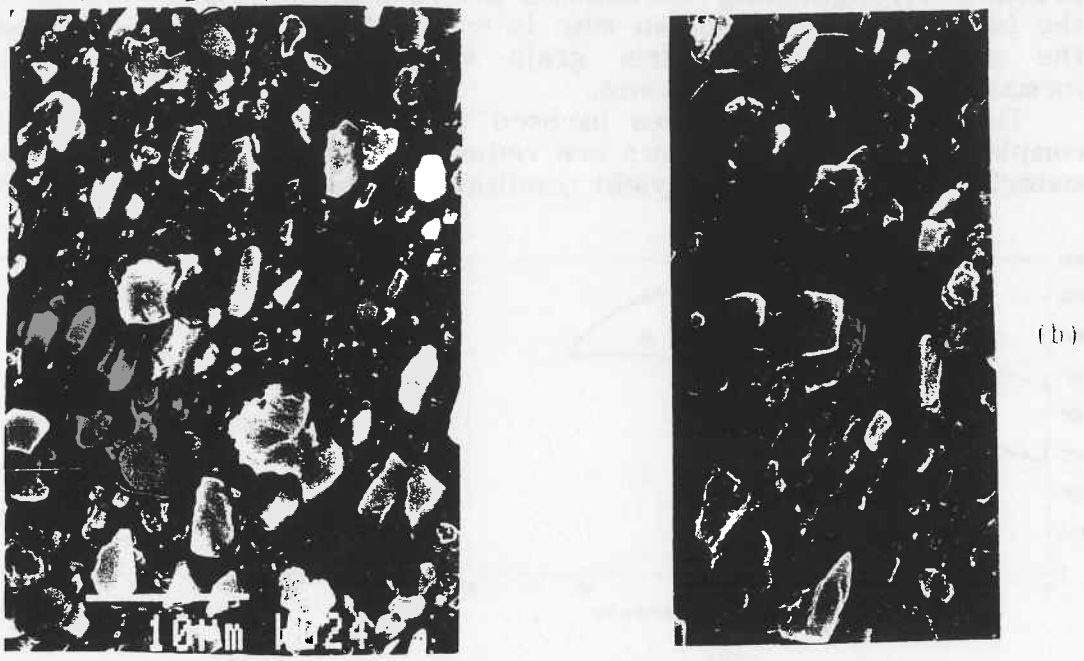

(a) (b)

Fig. 5 Particle orientation and distribution following 20 & 120 s etching

2.3 Strengthening Mechanisms

The strengthening and stiffening effect of the particles is due to a combination of the following: (i) the creation of dislocations at the interface, (ii) spacing of particles impeding dislocation motion, (iii) reduced matrix grain size, (iv) sub-grain formation and (v) strain-induced load transfer from matrix to particle.

Internal stresses arise following cooling during heat treatment. This leaves the matrix in tension and the particle in compression so that inelastic strain is induced in the material around the particle. The local plasticity creates a dislocation field at the interface. The density of these dislocations, ρ, restrict further plastic flow so increasing the strength, σ, according to [6]:

$$\sigma = aGb\sqrt{\rho} \qquad (1)$$

where $0.5 < a < 1.0$ is a constant, G is the shear modulus and b is Burger's vector. The particle size, d, appears within Eq. 1 indirectly since ρ is inversely proportional to d. Thus, for a given volume fraction, V_f, the smaller the particle the greater will be the strength. An estimate of an increase in strength of 20 MPa arises from this source [7].

Orowan strengthening [8] relates to the spacing, L, of hard particles:

$$\sigma = 2Gb/L \qquad (2)$$

where for a given V_f, L is proportional to d. Thus as $\sigma \propto 1/d$, the contribution to strength from Eq. 2 is not likely to be more than 10 MPa for an mmc [7]. The matrix grain size, D, is reduced by particles acting as

nucleation sites during solidification. Hall and Petch [9] showed that the corresponding increase in strength is:

$$\sigma = K/\sqrt{D} \qquad (3)$$

where K = 0.1 MPa$\sqrt{m}$, is a constant for high angle boundaries and D may be estimated from the particle size and volume fraction in: $D = d(1/V_f - 1)^{3/4}$. Taking V_f = 0.017 and $d = 3 \times 10^{-6}$ m, Eq. 3 gives a greater increase of σ = 44 MPa. This source will account for the increased hardness observed where recrystallisation of the matrix grains is inhibited by particles.

The grain size is further reduced from the formation of sub-grains as dislocations are re-arranged into boundaries within grains (see Fig. 6). This is a recovery process driven by the energy stored within the distorted matrix at the interface. The strengthening effect may again be estimated from the Hall-Petch Eq. 3 when K = 0.05 MPa$\sqrt{m}$, for lower angle boundaries.

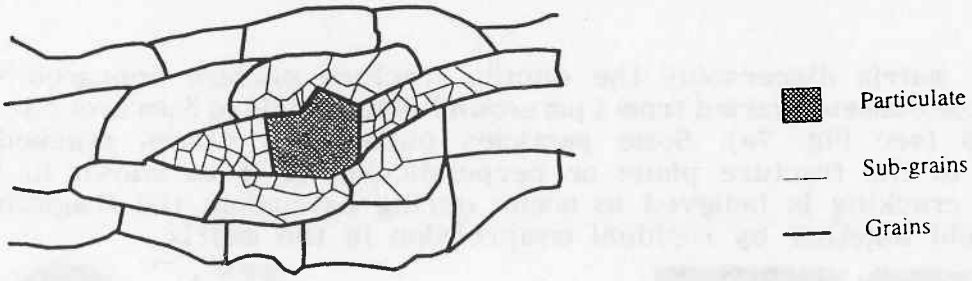

Fig. 6 Matrix sub-grain formation

The work hardening rate of an mmc is influenced by the dislocation network in two ways. Firstly, under a low applied tensile strain, ϵ, a load transfer occurs between the matrix and the particle. The increase in applied stress from this source is estimated to be [10]:

$$\sigma_{w1} = 9GV_f \, \epsilon/2 \qquad (4)$$

As the true strain is increased further dislocations are generated with an increasing degree of misfit between the matrix and particle. An estimate of the increased flow stress is given as [10]:

$$\sigma_{w2} = 5G\sqrt{(2V_f \, b/d)}\sqrt{\epsilon} \qquad (5)$$

Note, that these estimates of increased strength are relative to the matrix alloy which itself has been strengthened by precipitation hardening. Thus, summing Eqs 1 - 5 will provide a qualitative account of the increased strength arising from the addition of particulates to the alloy.

3. TENSION TESTS

Testpieces were machined longitudinally from the bar using a tipped tool. They were heat-treated with oversized dimensions. Therafter, a 15 mm long central parallel section was reduced from 6.43 mm to 4 mm diameter with 2.5 mm transition radii to ensure that all tensile failures occurred within this gauge length. A rate of continuous straining of 14×10^{-4} s^{-1} was applied in an Instron 4206 machine. A strain gauge was bonded axially

to determine the elastic tensile modulus. Additional tensile tests were made on an aluminium alloy of equivalent composition to the matrix alloy (2124) using standard dumbell-shaped testpieces. Table 1 compares the strength and ductility of the three materials. It is apparent from this that the particulate increases strength and stiffness at the expense of ductility.

The mmc failure surfaces aligned with transverse planes. They revealed two sites of crack initiation: (i) at inclusions arising from processing and (ii) at surface defects produced from machining. Between the SiC particles

Table 1 Effect of SiC particulate on a 2124 Al alloy

Material	E/GPa	ϵ_{ft}/%	Y	σ_{ut}/MPa
Al-alloy	72	12	300	475
17% SiC	101	6	480	650
25% SiC	110	4	490	690

and the matrix dispersoids the ductile fracture surface appeared dimpled. The dimple diameter varied from 1 μm around dispersoids to 5 μm around particles (see Fig. 7a). Some particles pulled out, others cracked either parallel to the fracture plane or perpendicular to it as shown in Fig. 7b. Particle cracking is believed to occur during extrusion, the fragments then being held together by residual compression in the matrix.

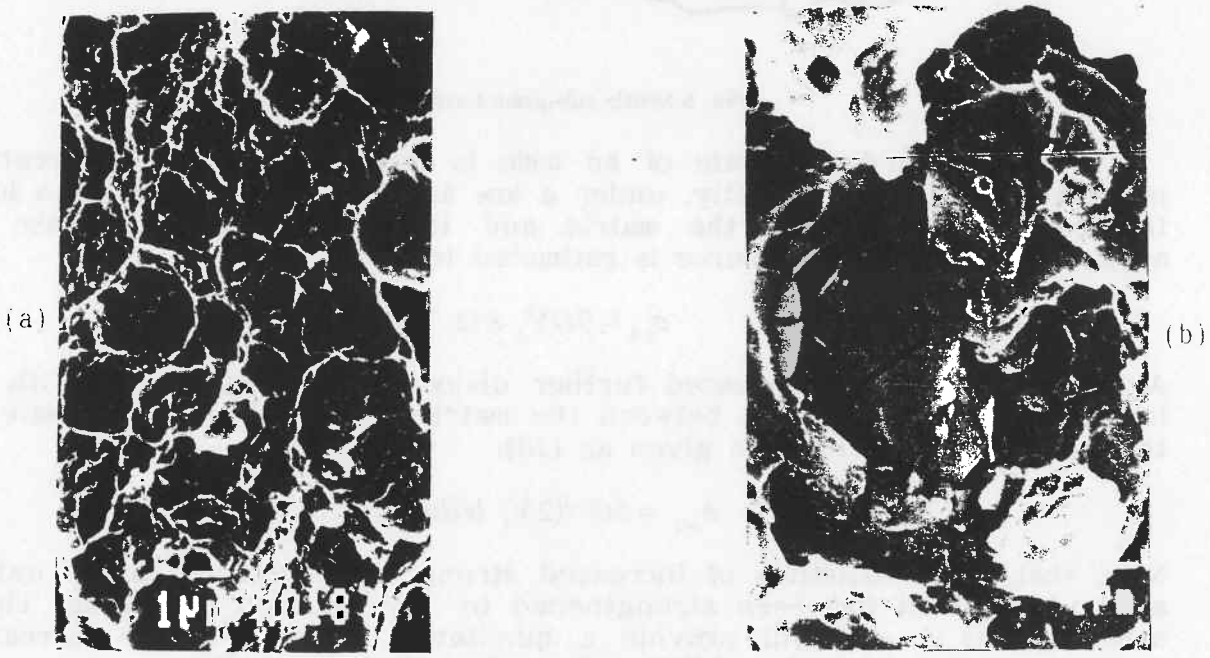

Fig. 7 Dimples and cracks within the fracture surface

4. COMPRESSION TESTS

Cylindrical testpieces, 10 mm long × 5 mm diameter, of the mmc and the matrix alloy, were compressed between sheets of ptfe and silicon grease in a Hounsfield tensometer. The length changes were measured following repeatedly unloading from the plastic range. Other testpieces were continuously strained to failure at rates of: 14, 69, 200 and 685 × 10^{-4} s^{-1} in an Instron machine. Some tests were interrupted for SEM examinations of

sectioned planes lying at 45° and 90° to the stress axis. Assuming a zero strain rate for the incremental tests, Table 2 summarises the results obtained for the two materials:

Table 2 Strain rate sensitivity of a 17% SiC mmc

$\dot{\varepsilon}/10^{-4}\,s^{-1}$	E/GPa	ε_{fc} /%	σ_{yc} /MPa	σ_{uc} /MPa	K	n	Matl
0	74	25	323	627	900	0.250	2124
0	104.8	13	433	830	1089	0.130	
14	103.8	29	517	880	1058	0.125	
69	103.4	27	509	840	1002	0.122	mmc
200	99.8	26	503	837	976	0.123	
685	101.1	27	467	802	959	0.132	

An number of empirical representations of the flow curve were examined. Log-log plots between the true stress and natural plastic strain (see Fig. 8) revealed that the flow behaviour conformed closely to Holloman's law [11]:

$$\sigma/\sigma_o = (\varepsilon^P/\varepsilon_o)^n \qquad (6)$$

where n is the hardening exponent, σ_o and ϵ_o are constants. Table 2 shows that n remains constant but the intercept decreases with increasing rate. Modifying Eq. 6 to account for strain rate sensitivity:

$$\sigma = K\,\dot{\varepsilon}^{\,m}\,\varepsilon^{\,n} \qquad (7)$$

The best fit to the data is found from taking K = 890, m = - 0.026 and n = 0.126. The negative index for an mmc in Eq. 2 is associated with a fall in the dislocation density as voids coalesce more rapidly under an increasing rate [12]. This implies that the flow process is time-dependent. The behaviour is unusual in that the material appears to be slightly stronger under a slower rate of straining. In contrast, a positive strain rate index is found for polycrystals where the dislocation density increases with plastic strain.

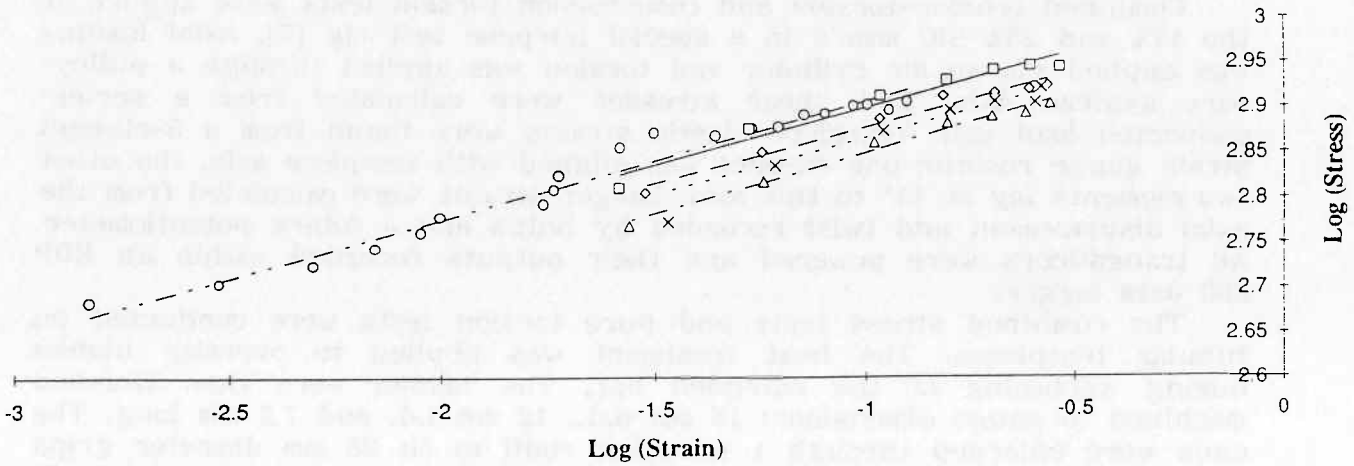

Fig. 8 Influence of strain rate upon compressive flow

(Key: — · — · —incremental, —— 14 × 10^{-4} s^{-1}, — — — 69 × 10^{-4} s^{-1}, - - - - 200 × 10^{-4} s^{-1}, — · — · —685 × 10^{-4} s^{-1})

All testpieces failed on the 45° plane of maximum shear. Exposed particles drag over this plane to produce furrows that obliterate the true fracture surface (see Fig. 9a). Interrupting the test and sectioning the testpiece along the two planes revealed voids between 1 and 10 μm in diameter (see Fig. 9b).

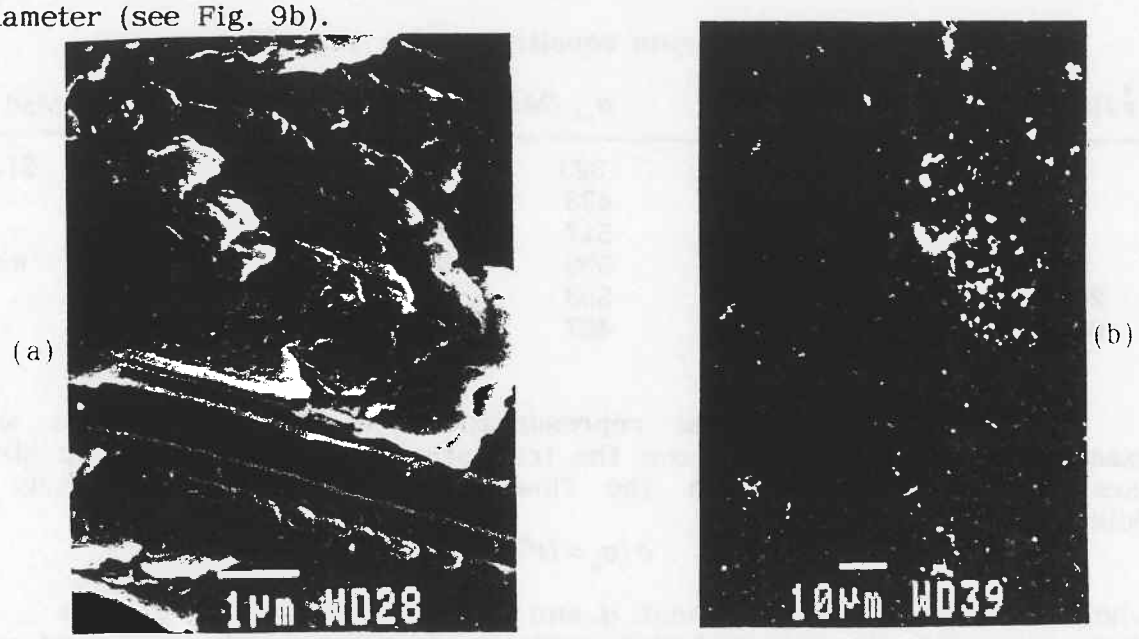

Fig. 9 Compressive fracture plane (a) after failure and (b) before failure

Voids nucleated between densely packed particles on all planes but only coalesced to their largest size, with an average number of 37 per mm² of a 45° plane. These voids form in the matrix under the high internal strains in regions of greatest particle density. Debonding of particles can occur as voids grow around them within a narrow band containing the fracture surface [13]. Large particles, 10 μm diameter or greater, are more likely than small particles to contain defects causing them to crack [14].

5. COMBINED LOADINGS

Combined tension-torsion and compression-torsion tests were applied to the 17% and 25% SiC mmc's in a special purpose test rig [7]. Axial loading was applied via an air cylinder and torsion was applied through a pulley-wire system. Axial and shear stresses were calculated from a series-connected load cell. Testpiece elastic strains were found from a 3-element strain gauge rosette; one element was aligned with testpiece axis, the other two elements lay at 45° to this axis. Larger strains were calculated from the axial displacement and twist recorded by lvdt's and a rotary potentiometer. All transducers were powered and their outputs recorded within an RDP 500 data logger.

The combined stress tests and pure torsion tests were conducted on tubular testpieces. The heat treatment was applied to oversize blanks during machining of the extruded bar. The blanks were then finished machined to gauge dimensions: 14 mm o.d., 12 mm i.d. and 7.5 mm long. The ends were enlarged through 1 mm fillet radii to fit 25 mm diameter grips with 18 mm flats [7]. The 1 mm wall thickness is representative of bulk behaviour in a material where the particulates are not greater than 5 μm diameter. After testing, additional miniature tension and compression testpieces were machined from the unstrained ends for testing on a Hounsfield tensometer.

5.1 The Yield Locus

In the determination of the yield locus from stepped stress paths, a small offset shear strain (0.05%) was used to determine the yield stresses. This allowed the same testpiece to be used for a number of torsional probes with different amounts of constant, elastic axial tension or compression. The offset strain definition of yield produces a small amount of plastic deformation with each probe. In a single testpiece this cumulative effect of strain history leads to deviations in which the points fall on either side of the flat region of the locus. Yield points were also determined from radial tests, from torsion, tension and compression at an equivalent offset strain value. Fig. 10 compares the initial yield points obtained from all loading paths on the 17% material with a theoretical von Mises yield locus [15]. This locus is given by:

$$\sigma^2 + 3\tau^2 = \sigma_o^2 \tag{8}$$

where σ_o = 490 MPa is the tensile yield stress of this material.

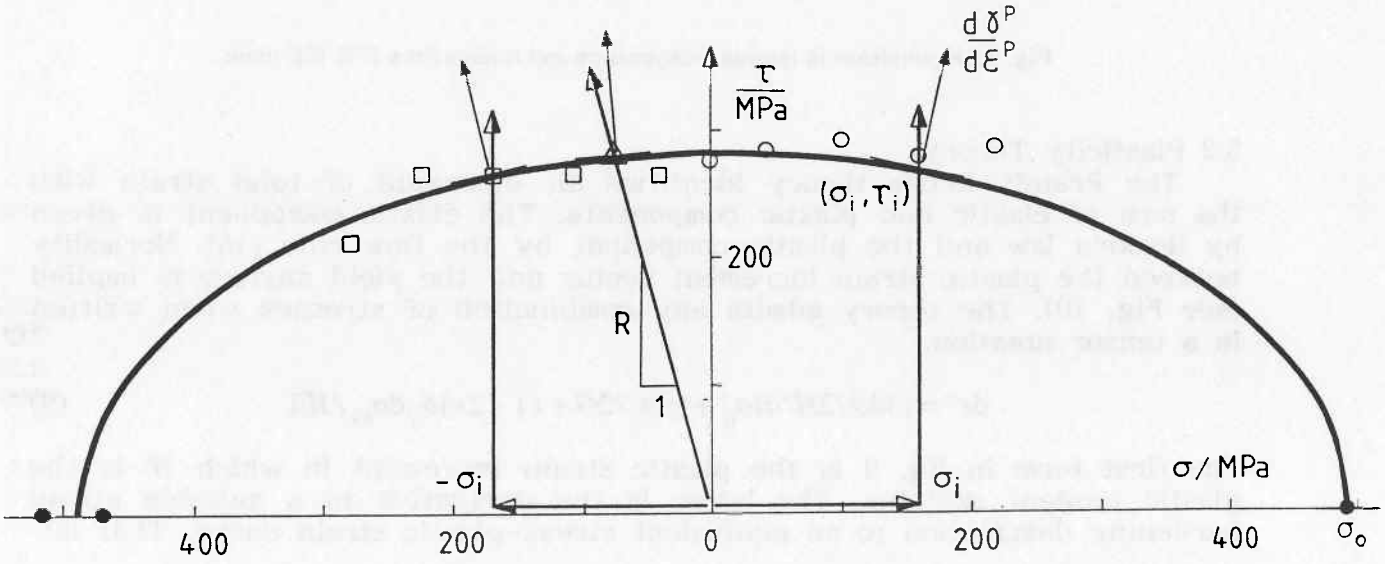

Fig. 10 Yield locus for mmc showing stress paths and normality

Tension, compression and torsion tests may also be used to examine the appropriateness of a Mises potential for subsequent plasticity. If this is so a Mises definition of equivalent stress and strain gives a single flow curve. This implies that plots of true stress versus natural plastic strain for tension and compression should coincide. These, in turn, should coincide with a torsion curve when its axes are converted to equivalent stress and plastic strain ($\sigma = \sqrt{3}\tau$, $\epsilon^P = \gamma^P/\sqrt{3}$). The double log-plot in Fig. 11 compares the equivalent flow behaviour for incremental loading under each mode.

The tensile and compressive flow behaviour is similar but the strains are far greater than was achieved from torsion (≈ 1%). By far the greatest strains can be achieved from compression (≈ 30%). The equivalent strains from torsion lie in a range lower by two decades. Points from all tests lie on a single line for which Hollomon's constants (Eq. 6) are: n = 0.104 and ϵ_o = 1.65 × 10^{-3}. This similarity in strain hardening appears to be independent of different modes of deformation. Transverse tensile failure limits the maximum strain to 6% while shear sliding along 45° planes provides a five-fold increase in axial compressive strain. A sudden transverse failure under torsion limited the amount of shear strain to between 1 and 2%.

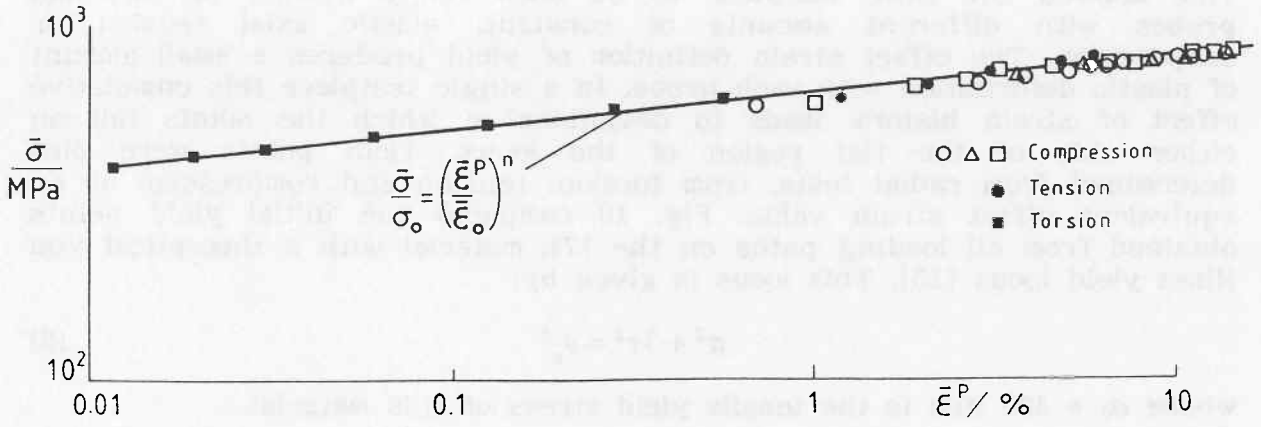

Fig. 11 Equivalence in tension, compression and torsion for a 17% SiC mmc

5.2 Plasticity Theory

The Prandtl-Reuss theory identifies an increment of total strain with the sum of elastic and plastic components. The elastic component is given by Hooke's law and the plastic component by the flow rule [16]. Normality between the plastic strain increment vector and the yield surface is implied (see Fig. 10). The theory admits any combination of stresses when written in a tensor notation:

$$d\varepsilon^t = (3d\bar{\sigma}/2H'\bar{\sigma})\sigma_{ij}' + [d\sigma_{ij}'/2G + (1 - 2\nu)\delta_{ij}d\sigma_{kk}/3E] \tag{9}$$

The first term in Eq. 9 is the plastic strain increment in which H' is the plastic tangent modulus. The latter is the derivative to a suitable strain hardening description to an equivalent stress-plastic strain curve. That is:

$$\bar{\sigma} = H(\int d\bar{\varepsilon}^P), \quad H' = d\bar{\sigma}/d\bar{\varepsilon}^P \tag{10a,b}$$

where $\bar{\sigma}$ and $\bar{\varepsilon}^P$ are given by the corresponding Mises definitions;

$$\bar{\sigma} = \sqrt{(3/2)}\sqrt{(\sigma_{ij}'\sigma_{ij}')}, \quad \bar{\varepsilon}^P = \sqrt{(2/3)}\sqrt{(\varepsilon_{ij}^P\varepsilon_{ij}^P)} \tag{11a,b}$$

Using a deviatoric stress tensor implies that hydrostatic stress does not influence the flow stress. For this to occur the material must remain plastically incompressible. The material's compressibility is attributed solely to elasticity. Thus, within the bracketed term ([ ]) of Eq. 9 the elastic component of strain is the sum of a shear and volumetric components where E, G and ν are the usual elastic constants. The present study requires a reduction of Eq. 9 to one axial stress and one shear stress. This gives the total axial and shear strain increments as [17]:

$$d\varepsilon^t = (d\bar{\sigma}/H'\bar{\sigma})\sigma + d\sigma/E \tag{12a}$$

$$d\gamma^t = (3d\bar{\sigma}/H'\bar{\sigma})\tau + d\tau/G \tag{12b}$$

The current equivalent stress, $\bar{\sigma}$, defines a flow potential that is assumed to be an inflation of the initial locus. Eq. 8 becomes;

$$\sigma^2 + 3\tau^2 = \bar{\sigma}^2 \tag{13}$$

where $\bar{\sigma}$ follows from the strain hardening law (Eq. 10a). Differentiating Hollomon's Eq. 6 gives the plastic tangent modulus:

$$H' = (n\sigma_o/\epsilon_o)(\bar{\sigma}/\sigma_o)^{(n-1)/n} \tag{14}$$

where σ_o and ϵ_o are respectively the stress and strain at yield and n is the gradient of the double-log plot in Fig. 11. The integration of Eqs 11a,b to give the total axial and shear strain components, ϵ^t, γ^t, will depend upon the stress path as will now be shown.

5.3 Radial Loading

A radial path is one in which the two stresses increase proportionately when loading a material into the plastic range. Referring to Fig. 10, the stress gradient $R = \tau/\sigma$. Substituting from Eqs 13b and 14b and introducing the normalised stresses: $S = \sigma/\sigma_o$ and $T = \tau/\sigma_o$, Eqs 12a,b integrate to total strains:

$$\epsilon^t = (\epsilon_o/n)(1 + 3R^2)^{(1-n)/2n} \int_{T_i}^{T} S^{(1-n)/n}\, dS + (\sigma_o/E)\int_0^S dS \tag{15a}$$

$$\gamma^t = (3R\epsilon_o/n)(1 + 3R^2)^{(1-n)/2n} \int_{S_i}^{S} S^{(1-n)/n}\, dS + (\sigma_o/G)\int_0^T dT \tag{15b}$$

The elastic strain components (final terms in Eqs 15a and b) contribute to the total strain under all stresses (S, T). Plasticity (first term) commences from the stress state at yield (S_i, T_i), i.e., where the path intersects the yied locus. With these normalised states defining the upper and lower limits to each of the first integrals, Eqs 15a,b lead to:

$$\epsilon^t = \epsilon_o(1 + 3R^2)^{(1-n)/2n}\,(S^{1/n} - S_i^{1/n}) + \sigma_o S/E \tag{16a}$$

$$\gamma^t = 3R\epsilon_o(1 + 3R^2)^{(1-n)/2n}\,(S^{1/n} - S_i^{1/n}) + \sigma_o T/G \tag{16b}$$

Substituting $n = 0.104$, $\sigma_o = 490$ MPa and $\epsilon_o = 1.65 \times 10^{-3}$ in Eqs 16a,b allow for the predicted flow behaviour to be compared with an experiment for which $R = 3.68$ in combined tension-torsion (see Fig. 12). The material behaves elastically while the stress state lies within the initial yield locus. The gradients of the linear paths define the elastic moduli in compression and shear: $E = 133$ GPa and $G = 45.5$ GPa. Plasticity commences when the stresses are: $S_i = (1+3R^2)^{-\frac{1}{2}} = 0.155$ and $T_i = RS_i = 0.57$. Substituting into Eqs 8a,b gives the total axial and shear strains in the plastic region. It is seen that while the theory (the u-curves) overestimates the stress and strain observed. The radial test was taken to fracture but the material is more brittle than the theory can admit. This suggests a modification using a damage parameter (see section 7.3). Dividing the first terms within Eqs 16a,b, shows that a radial path predicts a linear plastic strain path with gradient path $\gamma^p/\epsilon^p = 3R$. This behaviour follows from the rule of isotropic hardening where the initial yield locus expands, retaining its shape and orientation, to contain the current stress point. Radial loadings [15] confirmed that the strain path directed along the normal to the locus at the current stress point (see Fig. 10). Thus, void damage does not affect the ratio between the strain increments.

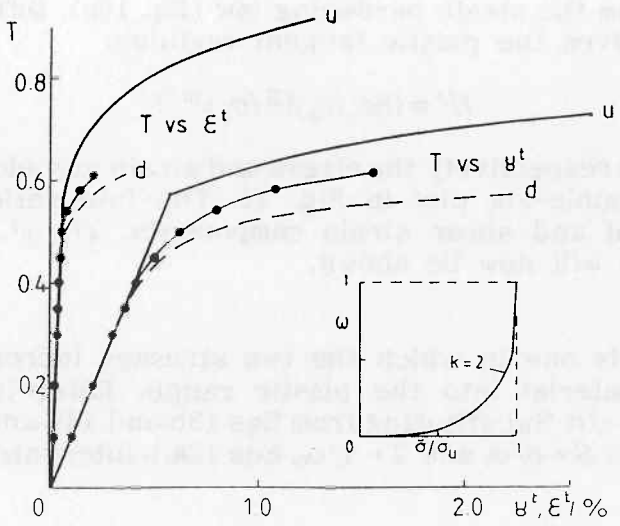

Fig. 12 Axial and shear flow under a radial path (17% SiC)
(Key: u - undamaged, d - damaged, ——●—— experiment)

5.4 Stepped Loading

The stepped paths (see Fig. 10) maintain an initial elastic axial stress, σ_i, constant either in tension or in compression while the shear stress is increased. Substituting Eqs 13b and 14b into Eqs 12a,b provide the two total strain integrals in dimensionless forms:

$$\varepsilon^t = (3\varepsilon_o S_i/n)\int_{T_i}^{T} (S_i^2 + 3T^2)^{(1-3n)/2n}\, T\,dT + (\sigma_o/E)\int_0^{S_i} dS \qquad (17a)$$

$$\gamma^t = (9\varepsilon_o/n)\int_{T_i}^{T} (S_i^2 + 3T^2)^{(1-3n)/2n}\, T^2\,dT + (\sigma_o/G)\int_0^{T} dT \qquad (17b)$$

where $(S_i^2 + 3T_i^2) = 1$. Integrating Eqs 17a,b:

$$\varepsilon^t = [\varepsilon_o S_i/(1-n)][(S_i^2 + 3T^2)^{(1-n)/2n} - 1] + (\sigma_o/E)S_i \qquad (18a)$$

$$\gamma^t = [3\varepsilon_o/(1-n)][T(S_i^2 + 3T^2)^{(1-n)/2n} - T_i - \int_{T_i}^{T} (S_i^2 + 3T^2)^{(1-n)/2n}\,dT] + \sigma_o T/G \qquad (18b)$$

The integral remaining in Eq. 18b must be solved numerically since the power is non-integer. With constant compression σ_i = - 260MPa, we have S_i = - 0.531 and T_i = 0.489. Making similar substitutions as before Eqs 18a,b predict the component stress-strain curves shown in Fig. 13. The first diagram shows that the initial elastic axial strain σ_o/E remains constant while the shear stress increases within the yield locus. The second diagram shows that the material responds elastically to the increasing shear stress

where the gradient defines the shear modulus. Plasticity in both axial and shear strain components commences at the intersection between path AB and the yield locus; σ_i = - 260 MPa and τ_i = 239.6 MPa (inset). The (—●—) superimposed test data in Fig. 13 shows some contrasting behaviour.

Firstly, there is not so clear a division between elastic and plastic behaviour. The axial strains were constant initially but departed sooner that the theory. Consequently, the yield point and the modulus are less clearly defined. Secondly, modifications to the theory are again required to account for loss in stiffness and low fracture strain due to void damage.

Eqs 18a,b show further that under a stepped path we should not expect a constant ratio between the plastic components of strain. That this was confirmed experimentally [15] adds support to combining the rules of normality and isotropic hardening for outward loading paths.

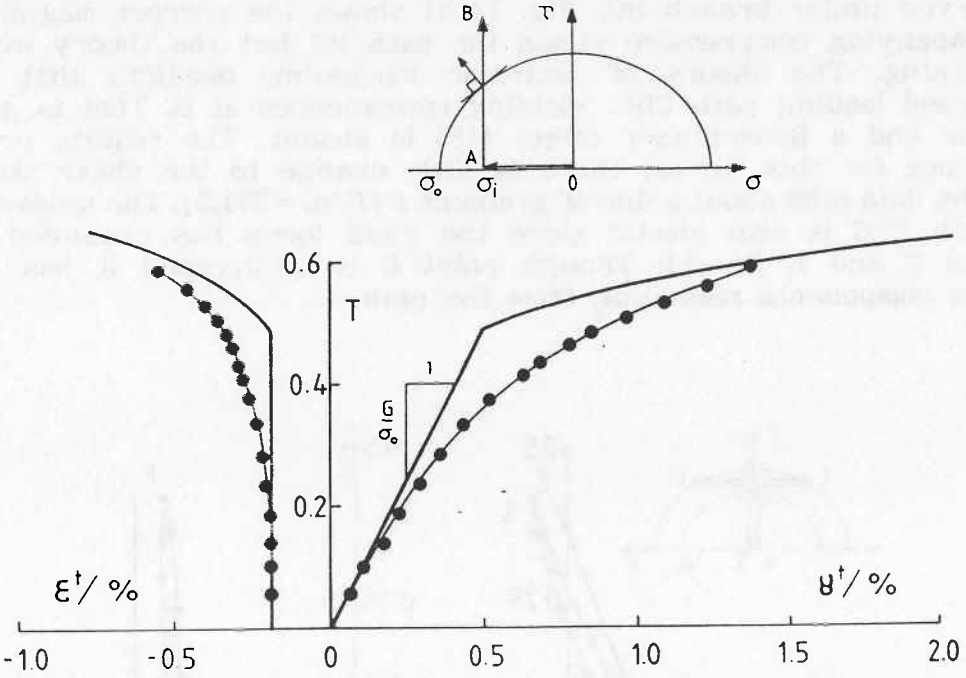

Fig. 13 Axial and shear flow under a stepped path (25% SiC)

5.5 Reversed Loadings

In the second stepped path, an initial plastic shear stress, σ_i = 296 MPa, was held constant. The testpiece was then probed alternately in compression and tension to a stress level of ± 246 MPa. Eqs 12 - 14 provide the two total strains for path ABC in the dimensionless forms:

$$\epsilon^t = (\varepsilon_o/n) \int_0^S (S^2 + 3T_i^2)^{(1-3n)/2n} S^2 \, dS + (\sigma_o/E) \int_0^S dS \qquad (19a)$$

$$\gamma^t = (3\varepsilon_o T_i/n) \int_{T_i}^T (S^2 + 3T_i^2)^{(1-3n)/2n} S \, dS + (\sigma_o/G) \int_0^{T_i} dT \qquad (19b)$$

Integrating Eqs 19a,b:

$$\varepsilon^t = [\varepsilon_o/(1-n)][S(S^2+3T_i^2)^{(1-n)/2n} - \int_0^S (S^2+3T_i^2)^{(1-n)/2n}\,dS] + (\sigma_o/E)S \qquad (20a)$$

$$\gamma^t = [3\varepsilon_o T_i/(1-n)][(S^2+3T_i^2)^{(1-n)/2n} - 3T_i^2] + \sigma_o T_i/G \qquad (20b)$$

The integral remaining in Eq. 20a is solved numerically for T_t = 0.604 allowing the limits for S to reach 0.5 in tension and compression. Here G = 48.1 GPa was found from the initial torsional loading path AB. Eqs 20a,b predict the component stress-strain curves shown in Figs 14a,b.

Fig. 14a shows that the theory reproduces the increase in shear strain observed under branch BC. Fig. 14(b) shows the correct magnitude in the accompanying compressive strain for path BC but the theory overestimates hardening. The theory of isotropic hardening predicts that under the reversed loading path CDE, yielding recommences at E. That is, path CDE is elastic and a Bauschinger effect [18] is absent. The results provide some evidence for this. In (a) there is little change to the shear strain and in (b) the data falls about a line of gradient E (E/σ_o = 271.5). The unloading branch EFG is also elastic since the yield locus has expanded to contain points C and E (inset). Though point G is unstressed it has two plastic strain components remaining from the path.

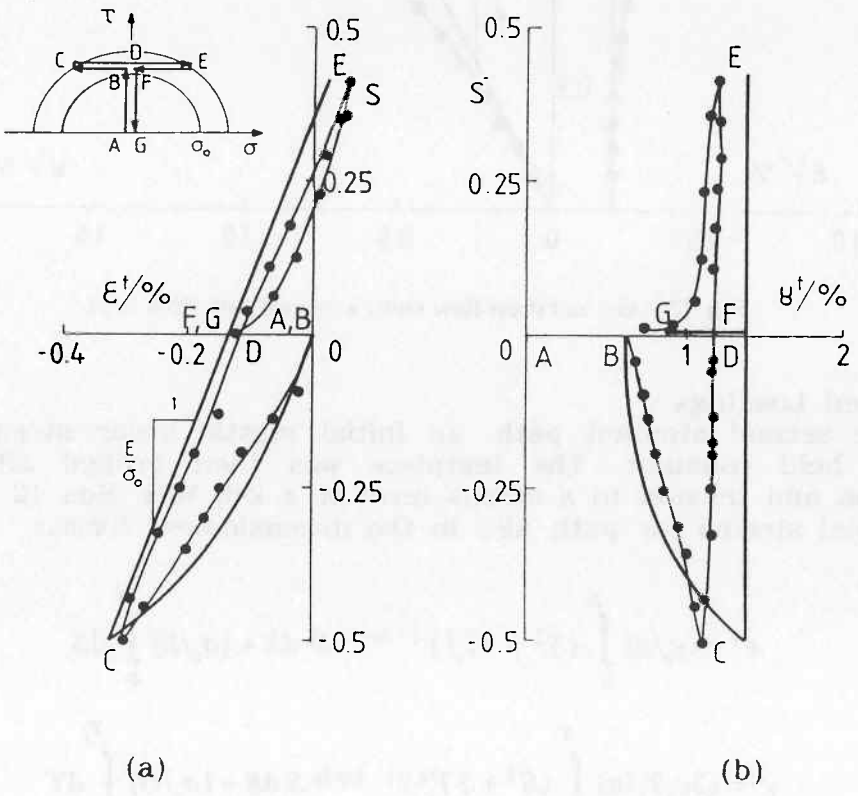

Fig. 14 Axial and shear flow under a reversed loading path (25% SiC)

6. RESIDUAL STRESSES

This section interprets the behaviour observed from the residual stress present in the material. Internal stresses arise in quenching from the solution treatment temperature of 505°C. They result from the difference in the expansion coefficients between the matrix and particle (23.5×10^{-6} and 4.5×10^{-6} K^{-1} respectively). Since $\alpha_{Al} > \alpha_{SiC}$, the matrix is left in tension and the particle in compression [19]. The quenching induces inelastic strain in the material around the particle so creating dislocations at the interface. If the residual stress around regular shaped particles is hydrostatic it is unlikly to affect flow stresses in tension and compression significantly. However, the relative sense of residual deviators and the applied system is likely to be crucial to the deformation behaviour of an mmc. The dislocation field existing in the strained material was created under tension. This field is thus more mobile under compression than under tension. Figs 15a,b show that the matrix residuals at state R are identified with partial unloading from within the plastic region of the matrix. Superimposed upon R are the flow curves from subsequent tensile and compressive loading.

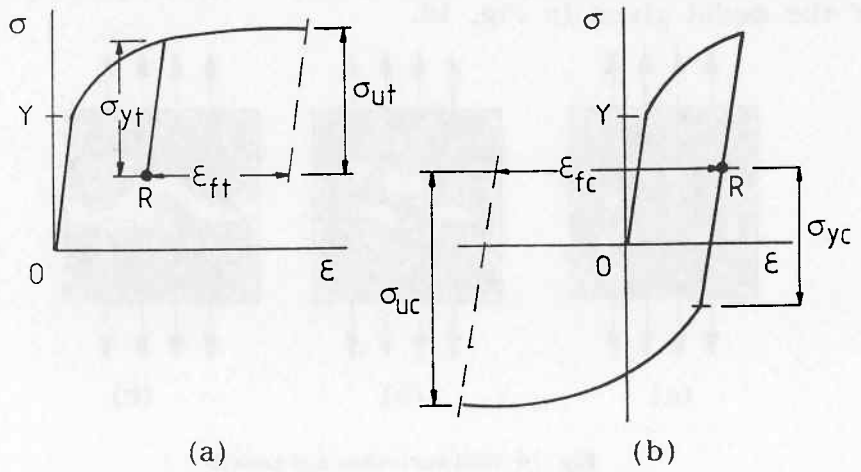

Fig. 15 The residual stress-strain state in the matrix

Taking R as the datum of subsequent stressing shows that the yield strengths, σ_{yt} and σ_{yc}, are comparable. The loss of some elasticity under tension ($\sigma_{yt} < Y$) is matched by a reduction in the reversed yield stress from the Bauschinger effect [18]. With continued deformation in each direction, the maximum ordinate will equalise about the stress-free origin, O, of each diagram. The applied stress must be taken relative to R, when the model predicts a slightly greater ultimate strength under compression ($\sigma_{uc} > \sigma_{ut}$). Similarly, it may be assumed that the material strains by the same amount in both directions relative to O. Thus, relative to R, a greater fracture strain will be observed from compression ($\epsilon_{fc} > \epsilon_{ft}$). The difference in the fracture strains will depend upon how far R lies along the tensile curve. In fact, much of the tensile ductility may be already be exhausted from processing and treatment. In practice, even larger differences in these fracture strains may arise through different failure modes operating. For example, the present study shows that shear sliding in compression and transgranular cracking in tension provide the fracture paths for linking voids. Under these conditions Fig. 11 quantifies differences in strength and ductility between each mode for a strain rate of 14×10^{-4} s^{-1}.

7. FRACTURE MECHANISM

7.1 Void Nucleation and Growth

The absence of decohesion in the tensile failures is due to a very high bond strength, the latter being close to the strength of the particle (1.7 GPa). There was also an absence of tensile necking. SEM examinations showed that damage was confined to a narrow band since few stable voids existed beyond it. Thus, void nucleation is critical to the mechanism of coalescence which leads to fracture. Voids do not exist already in the matrix. In order for them to nucleate the stress levels must be high enough to attain the energy levels required. Initially, much of the work of deformation is absorbed in creating dislocations at the interface. The internal stress field will continue to relax by the formation of secondary dislocations. These dislocations pile up between particles until they become effective barriers to their further motion. Barriers are also presented from the neighbouring dislocation fields around closely-spaced particles. At this point the local stress rises rapidly to nucleate voids in the matrix material around particles with a dense distribution. The appearance of voids on the fracture surface confirms that voids serve to propagate a crack in the manner of the model given in Fig. 16.

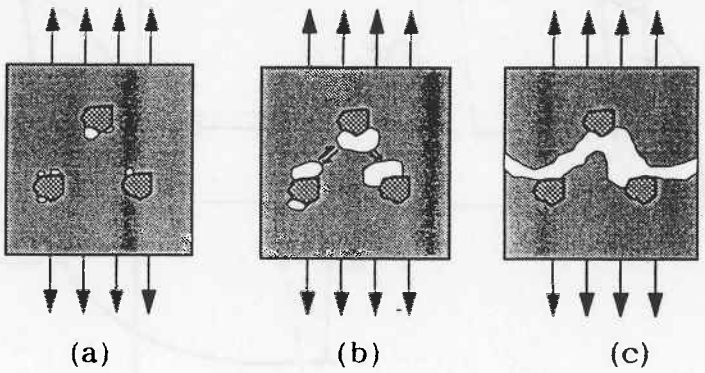

Fig. 16 Void nucleation and growth

This shows that: (a) voids first nucleate at the interface, (b) they then grow under the applied strain to a critical size, when in (c), the matrix fails in a brittle manner. In fact, voids may coalesce instantaneously under the opening stressses around their ends. Within this process the particle size, spacing and distribution play an important role in characterising the strength of an mmc.

7.2 Acoustic Emissions

Acoustic emissions depend upon the sudden changes in stress that accompany fracture. Higher emissions would be expected from particle fracture than from void formation [20]. The power spectral density, $X(f)$, was derived for tension and compression by amplifying the signal from a 0 - 2 MHz broad-band transducer then downloading to a computer. In both tests no emissions were observed until failure at which point they were captured in a 2 μs interval. Fig. 17 shows that the greatest emissions were observed at low frequencies of $f = 10^{-1}$ MHz in compression. It is believed that the higher emissions were due to friction between the 45° shearing surfaces. Since no medium to high frequency spectra were observed this implies little particle cracking. It is believed that the matrix material absorbed any emission due to void coalescence. In tension a larger burst accompanied failure consistent with rapid, simultaneous nucleation and growth of voids.

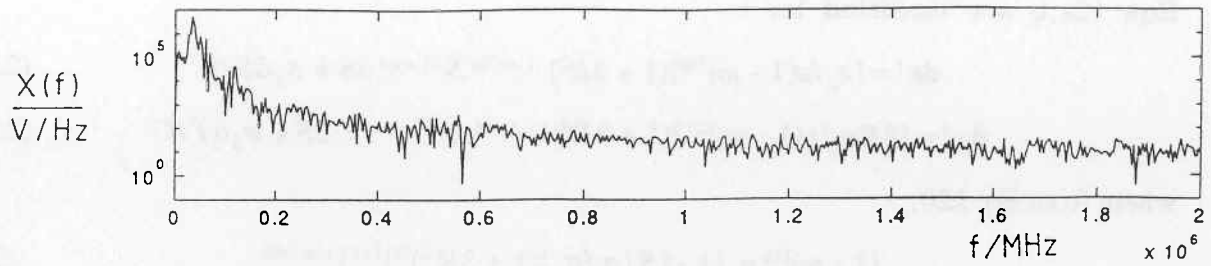

Fig. 17 Acoustic emissions accompanying compressive failure

7.3 Damage Parameter

Let us assume that damage is stress induced and that ωrepresents the loss in load bearing area varing from 0 in undamaged material to 1 at fracture [21]. This allows a damage derivative to be expressed in terms of true section stress as:

$$d\omega/d\sigma = B\sigma_t^k \tag{21}$$

where k and B are constants. Setting $\sigma_t = \sigma/(1 - \omega)$ in Eq. 21 leads to:

$$\int (1 - \omega)^k d\omega = B \int \sigma^k d\sigma$$

$$(1 - \omega)^{1+k} = 1 - B\sigma^{1+k} \tag{22a}$$

in which the constant of integration is found from $\omega = 0$ when $\sigma = 0$. At fracture $\omega = 1$ and $\sigma = \sigma_u$. Eq. 22 gives $B = 1/(\sigma_u)^{1+k}$ so that:

$$(1 - \omega)^{1+k} = 1 - (\sigma/\sigma_u)^{1+k}$$

$$\omega = 1 - [1 - (\sigma/\sigma_u)^{1+k}]^{1/(1+k)} \tag{22b}$$

Eq. 22b shows that the damage varies from 0 in an unstressed condition to unity when the ultimate stress is reached. For example, the inset diagram in Fig. 12 reveals the damage accumulated when $k = 2$. Let us apply this to the radial test. In the presence of damage the Hollomon law (Eq. 14) is written as:

$$\sigma = \sigma_o'(\varepsilon^P/\varepsilon_o')^n \tag{23a}$$

This implies that damage alters the yield stress and strain but not the hardening exponent. In the undamaged material assume that the same strain will be reached under an increased stress:

$$\sigma/(1 - \omega) = \sigma_o(\varepsilon^P/\varepsilon_o)^n \tag{23b}$$

Dividing Eqs 23a,b:

$$(1 - \omega) = (\sigma_o'/\sigma_o)(\varepsilon_o/\varepsilon_o')^n \tag{23c}$$

From Eqs 23a,c, H' becomes:

$$H' = d\sigma/d\varepsilon^P = (n\sigma_o/\varepsilon_o)(1 - \omega)^{1/n}(\sigma/\sigma_o)^{(n-1)/n} \tag{24}$$

Comparing Eq. 24 with Eq. 14b, it follows that the two strain increments in Eqs 12a,b are modified to;

$$d\varepsilon^t = [\varepsilon_o/n(1-\omega)^{1/n}](1+3R^2)^{(1-n)/2n} S^{(1-n)/n} dS + \sigma_o dS/E \qquad (25a)$$

$$d\gamma^t = [3R\varepsilon_o/n(1-\omega)^{1/n}](1+3R^2)^{(1-n)/2n} S^{(1-n)/n} dS + \sigma_o dT/G \qquad (25b)$$

where from Eq. 22b;

$$(1-\omega)^{1/n} = \{1 - [S(\sigma_o/\sigma_u)(1+3R^2)^{1/2}]^{1+k}\}^{1/n(1+k)} \qquad (26)$$

in which $S = \sigma/\sigma_o$ and $R = \tau/\sigma$. Combining Eqs 25a,b with Eq. 2 and then integrating each numerically provides the component stress-strain curves (d) in Fig. 12 for the damaged 17% SiC material. Clearly, these are nearer the observed behaviour where both the yield stress and fracture strains are reduced by void damage. Void growth measurement in tension are required to provide the k-value that fits the data more precisely.

8. CONCLUSIONS

The brittle tensile behaviour of an mmc is due to its notch sensitivity. Inclusions and poor surface finish raise the stress locally to provide the initiation site for a fracture with limited ductility. The fracture path is aligned with the major principal plane. The crack path through the matrix material consumes voids to link with pre-cracked particles. Upon reaching a critical crack size a transgranular failure occurs in the remaining ligament. Much of the void nucleation and growth occurs simultaneously at the instant of fracture though some voids do nucleate earlier. Compressive failures follow the plane of maximum shear by a similar void linkage mechanism. The voids nucleate in greater numbers in regions of high particle density. They form around particles in regions of dense, immobile dislocations when the local internal strain attains the limiting value for the matrix material. The stress levels required to yield and fracture the material under tension and compression are similar but there is a marked difference in their respective ductilities. The lower tensile strain shows that much of the available matrix strain has already been exhausted by the tensile residual strain arising from quenching.

The elements of the classical theory of plasticity apply to a particulate mmc. These are: (i) a Mises initial yield locus and a plastic potential, (iii) isotropic hardening and (iv) the normality rule. The absence of a significant Bauschinger effect is due to limited plasticity in the presence of residual stress. Deviations from the classical theory appear with the apparent sensitivity of plastic flow to the sense of an axial stress. The results indicate a modification to the classical theory to account for the tensile damage that accompanies plasticity in an mmc. A Katchanov parameter, normally used to express the loss in area due to brittle creep damage, can also express the varying degrees of damage resulting from the application of monotonic tension, compression and torsion alone and in combination. The principle employed is to let the stress-strain curve for a damaged material lie beneath that for undamaged material. Similar strains are reached in the two materials when the stress level in undamaged material is raised to a level that accounts for the loss in continuity ω within damaged material. Thus, a damaged material under an applied stress σ will strain by the same amount as an undamaged material under the increased stress $\sigma/(1-\omega)$.

REFERENCES

[1] B.S.Majumdar, A.H.Yegneswaran and P.K.Rohatgi, Strength and fracture behaviour of metal matrix particulate composites, Mat Sci and Engng, **68**, 85, 1984.

[2] T.W.Clyne and P.J.Withers, *An introduction to metal matrix composites*, Cambridge University Press, 1993.

[3] Prandtl,L. Ein Gedenkenmodell zur kinetischen Theorie der festen Korper, ZAMM, **8**, 85, 1928.

[4] Reuss,A. Berucksichtigung der elastichen Formanderungen in der Plastizitatstheorie, ZAMM, **10**, 266, 1930.

[5] von Mises,R. Mechanik der plastischen Formanderung von Kristallen, ZAMM, **8**, 161, 1928.

[6] N.L.Hansen, The effect of grain size and strain on the tensile flow stress of aluminium at room temperature, Acta Metall, **25**, 863, 1977.

[7] D.W.A.Rees and C.S.Stolworthy, Biaxial flow and fracture in a metal-matrix composite, Engineering Materials, Trans Tech, **86-87**, 77, 1993.

[8] E,Orowan, Internal stresses in metals and alloys, Inst of Metals, London, 451, 1948.

[9] Petch,N.L. The cleavage strength of polycrystals, Jl Iron and Steel Inst., **174**, 25, 1953.

[10] W.S.Miller and F.J.Humphreys, Strengthening mechanisms in metal matrix composites, Scripta Metall et Mater, 25, 33, 1991.

[11] J.H.Hollomon, Tensile deformation, Trans AIME, **162**, 268, 1945.

[12] S.Pickard, B.Derby, J.Harding anfd M.Taya, Strain rate dependence of failure in 2124 Al/SiC whisker composites, Scripta Metall, **22**, 601, 1988.

[13] R.K.Everett and R.J.Arsenault, *Metal-matrix composites: Mechanisms and Properties*, Academic Press Ltd, 1991.

[14] P.E.Magnusen, D.J.Srolovitz and D.A.Koss, A simulation of void linking during ductile fracture, Acta Metall Mater, **38**, 1013, 1990.

[15] Rees,D.W.A. and Liddiard, M. *Engineered Materials*, Proc IMF 11 (eds McHugh, P) Trans Tech, 1996.

[16] Levy,M. Memoire sur les equations generales CRAS **70**, 1323, 1870.

[17] Rees,D.W.A. Applications of classical plasticity theory to non-radial loading paths, Proc.Roy Soc. Lond, A410, 443, 1987.

[18] Bauschinger,J. Uber die Veranderung der Elastizitatsgrenze und des Elastizitatsmodulus verschiedener Metalle, CI, 289-348, 1881.

[19] Y.Flom and R.J.Arsenault, Deformation of SiC/Al composites, Jl of Metals, July, 31-34, 1986.

[20] P.M.Mummary, B.Derby and C.B.Scruby, Acoustic emission from particulate-reinforced composites, Acta Metall Mater, **41**, 1431, 1993.

[21] Katchanov,L.M. Time to failure under creep conditions, Izv. AN SSSR, OTN, No.8, 1958.